Extensional fault-propagation folds: mechanical models and observations from the Modoc Plateau, northeastern California

Ian R. White, Juliet G. Crider *

Department of Geology, Western Washington University, Bellingham, WA 98225, USA

Abstract

Extensional fault-propagation folds are produced by warping of material ahead of a growing normal fault. We use field observations of surface-breaking normal faults in the Modoc Plateau, California, in conjunction with three-dimensional linear elastic boundary element computer models, to address the mechanical controls on extensional fault propagation folds. Detailed topographic and structural maps of the near-tip regions of several kilometer-long faults reveal: throw decreases rapidly toward the tip, suggesting elliptical slip distributions; fault-parallel monoclinal folds are present beyond the tip, with axes offset into the hanging wall; and open fissures are common in the tip region. Parametric tests with the model show that the amplitude and form of folds at the fault terminations are influenced by slip distribution, fault dip, elastic properties of the rock, and the presence or absence of a blind portion of the fault. Models reproduce the form of observed folds to first order and suggest that the faults, both isolated and in relay zones, are probably blind for some lateral extent beyond the surface break.
© 2006 Elsevier Ltd. All rights reserved.

1. Introduction

Fault-propagation folds are produced by deformation of rock beyond the tip-line of lengthening faults. Research on the geometry, kinematics, and mechanics of fault-propagation folding has led to a better understanding of the growth of faults and fault systems, and to successful exploration for hydrocarbons near fault terminations (e.g. Mitra, 1990). The geometry and mechanics fault-propagation folds in contractional settings are well documented (e.g. Mitra and Wojtal, 1988; McClay, 1992). Of equal importance, but poorly documented, are fault-related folds produced in extensional tectonic environments. In the last decade, reviews of deformation around normal faults have illustrated the variety of folds possible in extensional environments (Schlische, 1995; Janecke et al., 1998). These include folds that occur around faults with irregular shapes (fault-bend folds), folds associated with variation in slip along faults (displacement-gradient folds), and fault-propagation folds.

Normal-fault propagation is accompanied by warping of material beyond the tip-line, resulting in an extensional fault-propagation fold (Fig. 1; Gawthorpe et al., 1997; Corfield and Sharp, 2000; Sharp et al., 2000; Khalil and McClay, 2002; Willsey et al., 2002). In this contribution, we investigate the manner in which propagation direction (lateral vs. vertical) affects surface deformation at the termination of normal faults. We consider effects of slip distribution, material properties, and fault interaction. We address extensional fault-propagation folding by: (1) detailed mapping of surface deformation near the tips of small surface-breaking normal faults in the Modoc Plateau, northeastern California; and (2) assessing possible mechanical controls on near-tip folds with three-dimensional linear-elastic boundary element models.

1.1. Previous work

Two classes of fault-propagation folds can be recognized. *Vertical* fault-propagation folds form ahead of upward-propagating dip-slip faults and are the result of the relative motion of material on either side of the fault (a class of 'forced folds'). The concept of fault-propagation folding was originally applied to vertical fault propagation in contractional settings, where slip on a thrust fault decreases up dip until shortening is accommodated by folding rather than faulting. *Lateral* fault-propagation folds form ahead of horizontally-propagating

---

* Corresponding author.
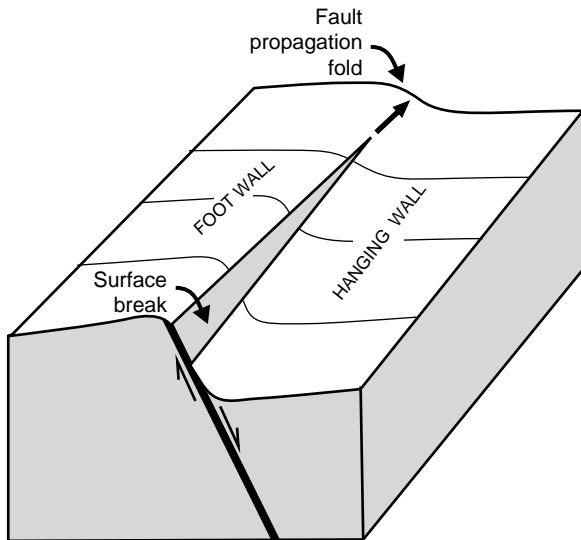*E-mail address:* criderj@cc.wwu.edu (J.G. Crider).

Fig. 1. Block diagram of warping beyond the tip-line (fault-propagation fold) produced by lateral and vertical propagation of a normal fault. A monocline forms above the blind, upwardly-propagating fault and/or ahead of the laterally-propagating fault. After Walsh and Watterson (1987), Schlische (1995) and Sharp et al. (2000).

dip-slip faults and are the result of warping of rock at the juncture of the footwall and hanging wall (Fig. 2). A lateral fault-propagation fold is not rooted in a blind fault, and its hinge is sub-perpendicular to the associated fault tip-line. Both classes of folds can change the local topography around near-surface faults, which, in turn, produces important controls on the pattern of erosion and deposition of sediments (Gawthorpe et al., 1997).

Field observations of extensional fault-propagation folds have come mainly from deformed pre- and syn-extensional strata associated with large normal fault systems in extended
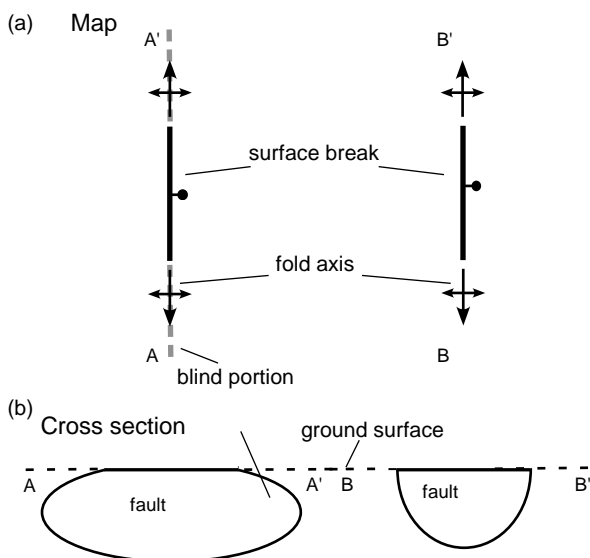

Fig. 2. Distinction between vertical and lateral fault-propagation folds at Earth's surface. (a) Vertical fault-propagation folds result from upward propagation of a blind fault, or a portion of a fault that is blind, toward the surface. (b) Lateral fault-propagation folds result from lateral propagation of a fault that breaks the surface completely along strike.

regions. Kilometer-scale fault-propagation folds have been recognized in the Gulf of California (Willsey et al., 2002), the Suez rift (Sharp et al., 2000), the Red Sea (Khalil and McClay, 2002), and from the Smørbukk area, mid-Norway based on 3-D seismic data (Corfield and Sharp, 2000).

Study of young surface-breaking normal faults allows for detailed investigations of relatively simple structures. Peacock and Parfitt (2002) examined fault linkage structures on the south flank of Kilauea Volcano, Hawaii where the shield volcano is actively deforming to accommodate gravity driven extension. Grant and Kattenhorn (2004) document normal-fault-related monoclines in southwest Iceland. Both sets of researchers demonstrate the importance of folding in normal-fault growth; they differ in their interpretation of the initiation and role of accompanying fissures.

A small pool of research focuses on using experimental and kinematic models to study extensional fault-propagation folds. Horsfield (1977) describes sandbox models of deformation above dipping normal faults, resulting in subsidiary faulting. Withjack et al. (1990) used aluminum blocks with an overlying clay layer to simulate forced folding. They found that strain is distributed in an upward widening monocline above a discrete normal fault surface. Using a 2-D trishear kinematic model, Hardy and McClay (1999) were able to successfully reproduce the results of clay analogue modeling.

A number of studies in recent decades have explored the mechanics of forced folds. Haneberg (1992) examines forced folding of compressible elastic strata over rigid basement blocks. Patton and Fletcher (1995) present a 2-D mathematical model for deformation of an incompressible layer overlying a relatively rigid basement fault of arbitrary dip. Johnson and Johnson (2002b) show the influence of fault geometry and cover anisotropy with 2-D mathematical models of cover over a rigid basement fault. All three of these approaches are limited to cross-section views of an infinitely long fault, and thus address only the geometry of vertical fault propagation (or drape) folds. In this study, we sacrifice mechanical complexity for three dimensions, allowing us to explore folds produced above or beyond the lateral tip lines of normal faults.

1.2. Geology of the Modoc Plateau

The Modoc Plateau volcanic-upland region of northeastern California (Fig. 3) provides an excellent location to observe surface deformation associated with normal faults. Miocene and younger normal faults break the surface through basalt and are exceptionally well preserved. Volcanic terrain such as the Modoc Plateau preserves surface deformation relatively well and is thus a common substrate for mechanical studies of faulting (e.g. Dawers et al., 1993; Dawers and Anders, 1995; Crider and Pollard, 1998; Crider, 2001). Additionally, the Modoc Plateau is sparsely vegetated in many areas, providing easy access and good exposure.

The Modoc Plateau is situated between the Basin and Range Province and the Cascades Volcanic Arc. The plateau is the southernmost part of a region of Miocene-to-Quaternary, flat-lying basaltic lava flows that extend northward into Oregon
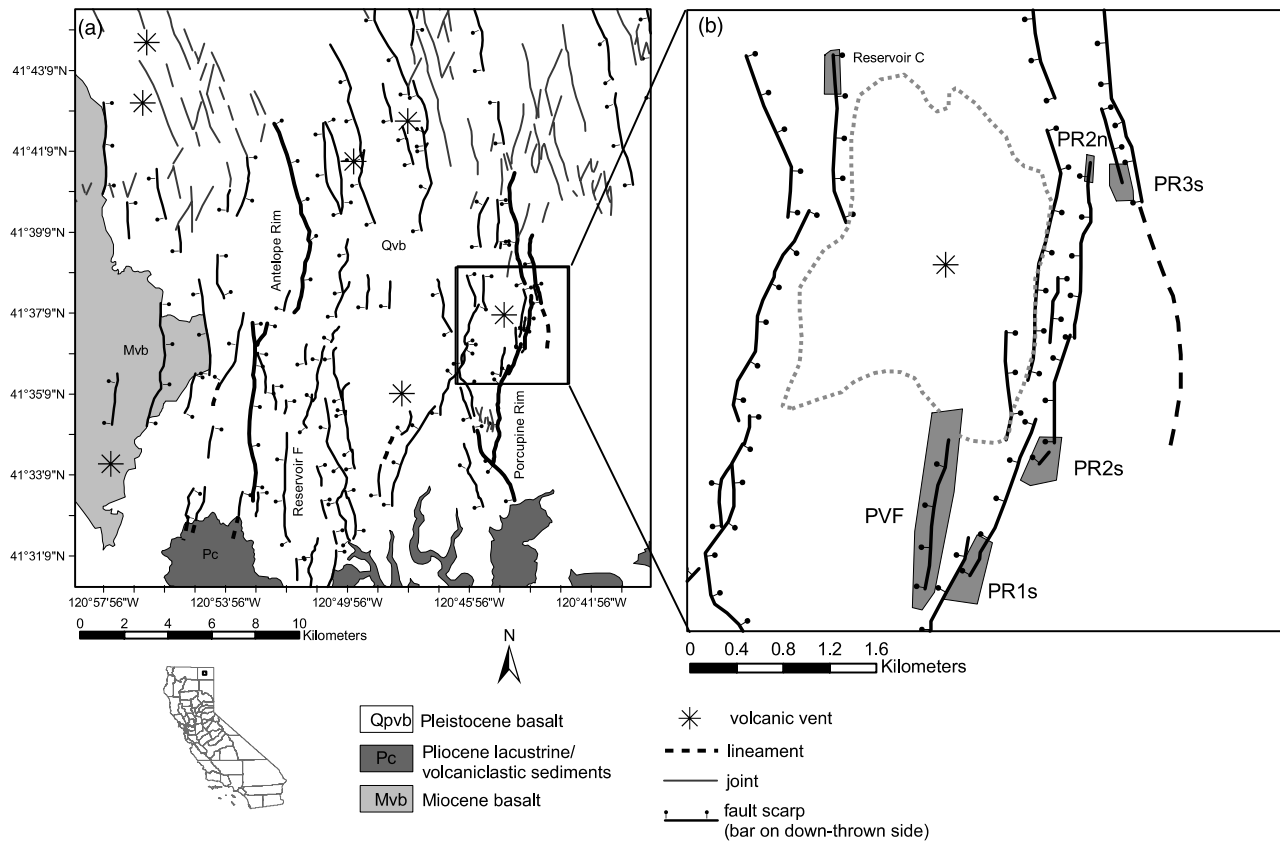
Fig. 3. (a) Regional fault map of study area based on aerial photo interpretation and geologic map of Gay and Aune (1958). Porcupine Rim and Antelope Rim are in bold. These large, antithetic faults bound the region of high-density normal faulting. (b) Porcupine Rim area, the focus of detailed mapping. Shaded areas with labels represent the extent of detailed survey for each scarp. Gray dotted line shows the extent of topography related to volcanic vent (star).

(Montgomery, 1988). To the west, Quaternary flows of the Medicine Lake, Mt Shasta, and Lassen Peak volcanic centers lie conformably above Modoc Plateau volcanics (McKee et al., 1983). To the east, the province is bounded by the east-dipping Surprise Valley normal fault and the Warner Mountains, a block of west-tilted Miocene volcaniclastic rock (Hedel, 1980).

We describe faults in the Devil's Garden Lava Field (McKee et al., 1983) of the Modoc Plateau. Quaternary normal faults in this region are generally north–northwest-trending (Jennings, 1994). Gentle anticlines are associated with many of the faults, and structural depressions in the area are generally filled with Quaternary sediments (Montgomery, 1988). Total thickness of the basalts mantling the Devil's Garden area has been observed in outcrop to be as much as 80 m in some areas, and may be much greater (McKee et al., 1983), with individual flows generally less than 10 m thick. The basalts are directly underlain by a thick sequence of tuffaceous lacustrine sedimentary rocks of the Alturas Formation (McKee et al., 1983). Although Pleistocene fossils have been found near the top of the Alturas Formation (Kramer, 1980), McKee et al. (1983) date the basalts at 5.3–10.5 Ma (K/Ar) (late Miocene to early Pliocene), with ages generally younging to the southwest. Controversy over the age of the Devil's Garden Basalts remains unresolved. Below the Alturas Formation lies a thick sequence of early Tertiary volcaniclastic rocks exposed in the Warner Mountains.

Late Cenozoic extension and related bimodal volcanism in the Modoc Plateau may be attributed to a combination of tectonic processes. First, the Plateau sits in a region just west of the Basin and Range, and its features may represent an encroachment of Basin-and-Range-style faulting into the Cascade Arc. Second, the Plateau is situated in a back-arc position relative to the modern Cascade Arc. The chemistry of the basalts shows back-arc basin affinity (McKee et al., 1983), and the onset of basaltic magmatism in the area may correspond to westward migration of Cascade volcanism (Montgomery, 1988). Finally, Blakely et al. (1997) recognize northeast-trending low gravity anomalies extending from modern volcanic centers in the Cascade Range, across northeastern California, and into Nevada and Oregon. They attribute normal faulting in the gravity lows (of which the Modoc Plateau is a part) to a pull-apart geometry resulting from transferring dextral shear in the Walker Lane Shear Zone to east–west extension in the southern Cascade Range.

The age of initiation of normal faulting in the region is not well constrained. It is possible that faults were active before and during eruption of the Devil's Garden lavas, but we do not observe any direct evidence for this in the field. In the absence of evidence to the contrary, we presume with some confidence that the *latest* motion on the faults described here post-dates the basalts, and that the topography of the basalt surfaces is a result

of post-emplacement deformation and not draping over an existing scarp.

2. Field observations

2.1. Regional fault map

A map of faults and joints in the southernmost region of the Devil's Garden province of the Modoc Plateau is presented in Fig. 3. The southern edge of the study area is bounded by the Pit River Valley. Two prominent normal faults, Porcupine Rim on the east and Antelope Rim on the west, define the longitudinal limits of the study area. The two faults have converging dips, continuous traces, and large displacements relative to other faults in the study area, bounding what may be a single large graben. The northern limit of the study area is marked by a transition from normal faulting to jointing.

The mapped region is characterized by north-striking normal faults and conjugate sets of northwest- and northeast-striking joints in otherwise flat-lying basalt (Fig. 4). Faults are generally segmented and show scarp relief up to 75 m. They commonly have converging dips and create small, alluvium-filled graben. In contrast, joints are linear and do not show any measurable offset at the air photo resolution. Examination of the joints in the field reveals that most do not show any throw, but a number appear to have been reactivated as faults and have throw of up to 2 m. Mean strike of the faults corresponds to that of the joints, suggesting that north-striking faults may result from linkage of NNW- and NNE-striking segments on reactivated joints. It is unknown whether the joints are pre-

existing structures that faults exploit, or if jointing is an early expression of fault growth. In addition to faults and joints, a number of volcanic centers dot the field area and are expressed as circular shield-shaped mounds of basalt with varying degrees of degradation. The diameters of the mounds range from 1 to 2 m. Faults commonly have arcuate traces where they intersect the mounds.

Slip surfaces are not apparent along any of the scarps investigated during this study. They are either quickly degraded once exposed, or the manner that slip occurs on the faults does not favor their production. Consequently, the absolute direction of slip for faults on the plateau is difficult to resolve. Additionally, the rocks in the hanging wall are rarely exposed, so mapping linear features across the scarps proved difficult. At one site we observe a flow boundary nearly perpendicular to the strike of faults. The faults show up to 20 m of throw at that location, but there is no measurable lateral offset of the flow boundary, indicating normal dip-slip (White, 2003).

Where basalt is exposed at the surface, it typically shows columnar jointing perpendicular to the upper surface, with column diameters ranging from 25 cm to 2 m. The basalt is also generally vesicular with up to 30% vesicles. Near the center of Porcupine Valley Fault, a contact between two basalt flows is exposed. The lower flow is topped by a thin ($\sim$20 cm) zone of very vesicular and ropy basalt. Below this thin vesicular cover, the basalt is columnar and moderately vesicular with vesicles virtually disappearing $\sim$1.5 m below the flow surface. If the overlying flow is of a similar thickness and character, this suggests that there has been no more than $\sim$1.5 m of erosion from the current surface.

2.2. Topographic maps of near-tip regions

Field data collected for this study consist of surface elevations (based on GPS and total station surveys) and structural observations from near-tip regions of surface-breaking normal faults in the Modoc Plateau. Elevation data were compiled to construct topographic maps of the near-tip regions and along-strike profiles of scarp fronts. These compilations, along with structural observations, help characterize the surface deformation in near-tip regions.

The topographic data were filtered so that only differential positions with estimated vertical precisions of $\pm$1.5 m or better were used for contouring. The vast majority of the points collected showed sub-meter precisions. After surveying, draft topographic maps were created and each tip region was visually inspected to assure that the maps were accurate representations of the landform. These data were merged with USGS 10-m digital elevation models at the margins of the surveyed areas.

A total of six near-tip regions of normal fault scarps in the Modoc Plateau were examined in detail. For the purposes of this study, a near-tip region extends from the last point where the scarp is marked by a cliff to the point where there is no longer any apparent topographic expression of the scarp. In an effort to simplify the study, only those faults with clearly
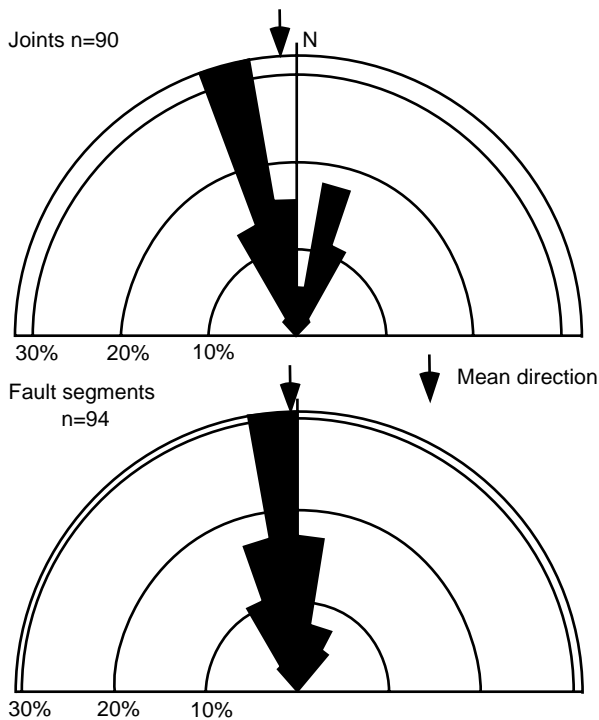

Fig. 4. Rose plot of joint and fault segment orientations for the study area. Mean directions are nearly identical for the two sets, but joints cluster in two groups slightly east and west of north.

identifiable tips were mapped in detail. The faults are given informal names for the sake of discussion.

2.2.1. Porcupine Valley

The Porcupine Valley Fault (PVF) is located just west of the more prominent Porcupine Rim structure, a 15-km-long normal fault system made up of east-stepping segments (Fig. 3). Although the PVF nearly parallels a strand of Porcupine Rim and the two are probably in mechanical interaction, they are not linked at the surface. The PVF is 1.3 km in length and both tips are well exposed. The scarp height is 15 m near the center and displacement decreases to zero in a uniform manner at both ends. The scarp faces west, creating a basin filled with alluvial sediments in the hanging wall and an uplifted plateau of exposed basalt in the footwall (Fig. 5a). A survey of the entire length of the fault was completed, along with more detailed surveys of the north termination, south termination, and a monoclinal structure near the center of the fault.

Mapping reveals that the fault is a collection of mostly right-stepping, north-striking segments connected by short (<100 m) northeast-striking segments (Fig. 6). Generally, the north-striking segments are vertical cliffs with rubble piles below (∼1/2 scarp height), while the northeast striking segments tend to have gentler and more uniform slopes, consisting primarily of unvegetated rubble.

Near the northern termination of the fault, the scarp dies out into a region of topographic relief with no cliff face. In this region, the fault trace is marked by a north-striking slope of unvegetated rubble. In some locations, unvegetated basalt, apparently intact with the bedrock, is exposed at the surface. These locations are marked by strike and dip measurements on the map. The surfaces dip gently toward the hanging wall with essentially uniform dips along strike. Surrounding this strip of exposed rock, the pavement of basalt is generally vegetated, with minor soil development in the spaces between columns. At the northern limit of the scarp, where only a gentle slope remains, there is a low relief (∼0.5 m) northeast-striking sinuous scarp ∼20 m long.

Near the southern termination of the fault, the scarp is heavily vegetated and more difficult to observe. Approximately 100 m from the end of the scarp, its configuration changes from a cliff with talus at its base to a vegetated talus slope. Within the talus slope, a north-trending fissure steps slightly to the west of the main structure. Where exposed, intact basalt surfaces dip gently towards the hanging wall, with their strikes parallel to the fault trace.

Near the center of the scarp, a large block (∼15×30 m) of intact basalt protrudes ∼6 m out of the hanging wall sediments. The block is located along a segment where the fault strikes northeast to accommodate a right-stepping geometry. Flow surfaces on the block strike parallel to the local trace of the fault and dip moderately towards the hanging wall, with dips increasing toward the hanging wall in the shape of a monocline. A cross-section through the monocline and onto the scarp reveals that the top of the block projects directly to the top of the scarp about a rotation point below the surface (Fig. 7a). The block is
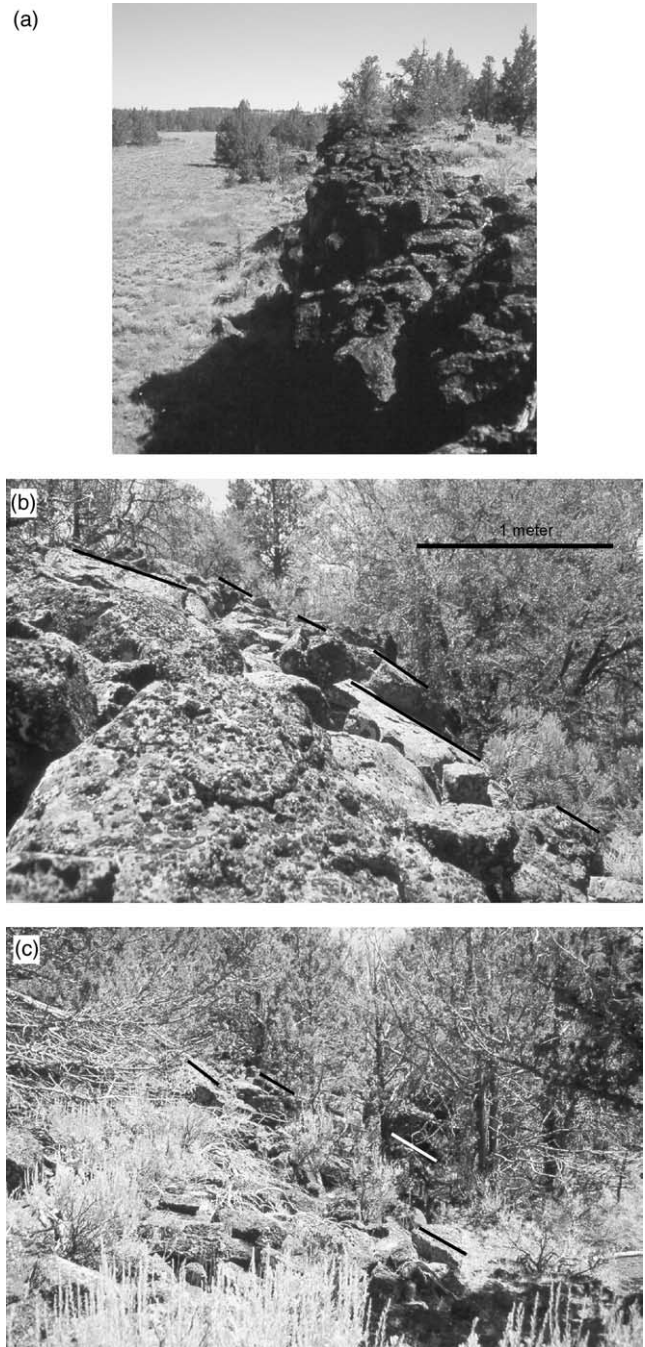
Fig. 5. (a) North-facing photo near the center of the Porcupine Valley scarp (PVF), where displacement is at a maximum, illustrating typical scarp morphology. The hanging wall is buried by a flat plain of alluvial sediments, and the footwall exposes basalt bedrock. A geologist (with GPS antenna) is shown on the footwall for scale. The scarp height at this location is 15 m. See Fig. 6 for location. (b) South-facing photo of the Porcupine Rim 1 (PR1) tilted hanging wall block (see Fig. 8 for location). Black lines highlight flow surfaces that are apparently intact and folded in a monocline. (c) South-facing photo of the vegetated rubble slope at the north termination of Porcupine Rim 2 (PR2n; see Fig. 8 for location). Short lines highlight flow surfaces.

separated from the main scarp by a linear trench ∼10–15 m wide and ∼3 m above the surrounding hanging wall surface.

The cliff face in this area of the fault exposes the contact between two basalt flows, an upper flow ∼4 m thick and
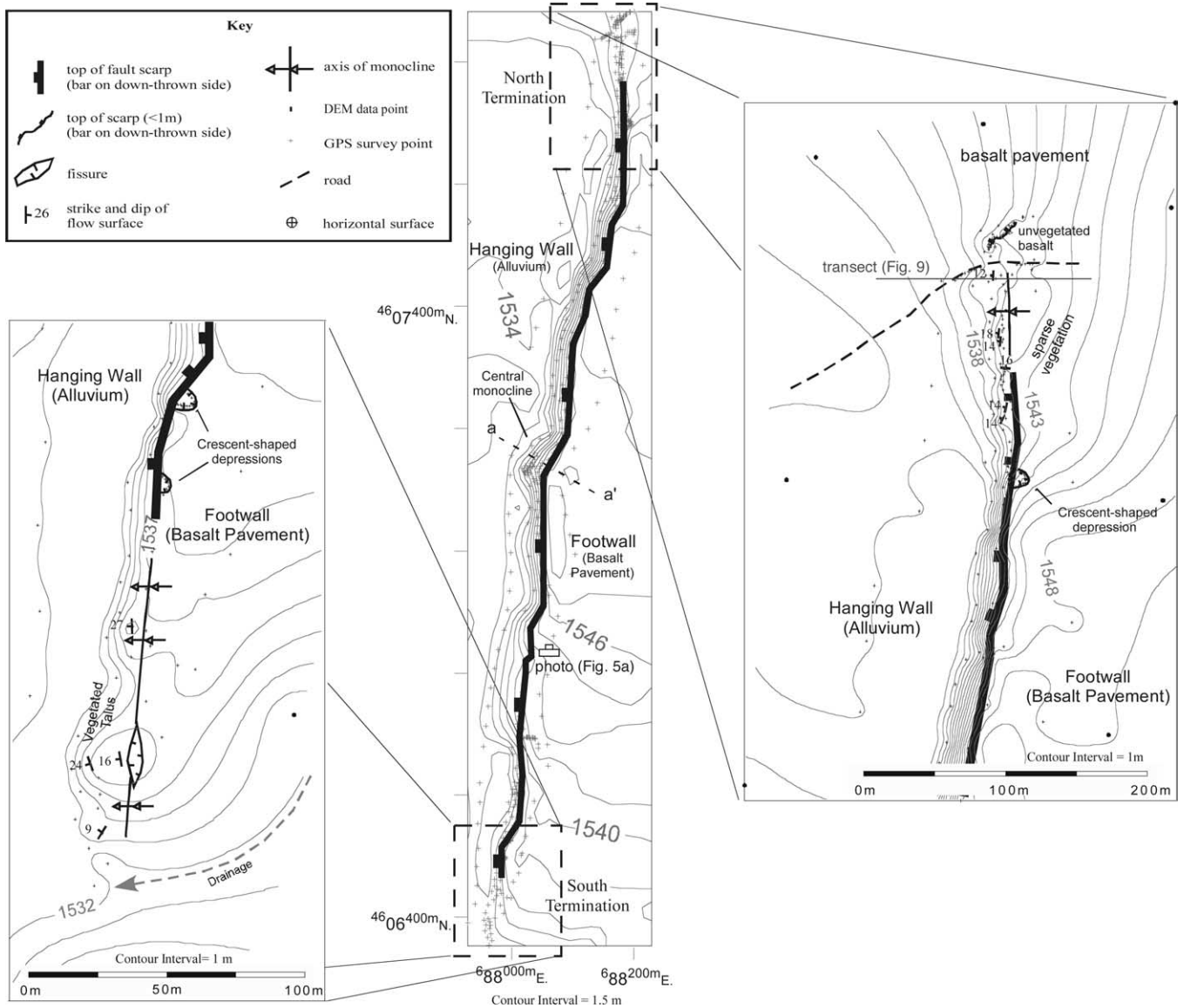
Fig. 6. Detailed topographic and structural maps of the Porcupine Valley Fault scarp.

a lower flow of unknown thickness. The contact is exposed on both the west and east sides of the trench separating the block from the main scarp. Just north of the block, basalt surfaces of the lower flow are exposed near the base of the scarp. The surfaces strike parallel to the fault scarp and dip moderately toward the hanging wall, indicating that the fold is kinematically linked to the fault.

2.2.2. Porcupine Rim 1

Porcupine Rim 1 (PR1) is the southernmost in a series of right-stepping fault segments at the center of the Porcupine Rim structure (Fig. 3). The total relief along the top of the scarp is 18 m, with maximum elevation offset toward the south tip. It is ~1.6 km long. The south termination of the fault was surveyed in detail (Fig. 8). In the footwall of this section of the fault, topographic contours parallel the trace of the fault. In the hanging wall, however, contours are oblique to the fault trace, reflecting the influence of the adjacent fault segment. The trace
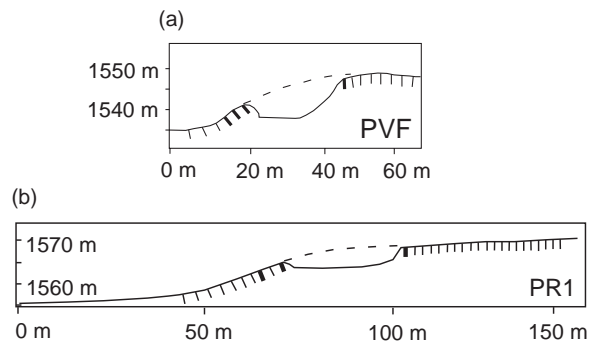

Fig. 7. Cross-sections perpendicular to fold axes for the PVF and PR1 central monoclines. There is no vertical exaggeration and the topography is based on GPS surveying. In the valleys between the fold and the main scarp, topography was adjusted to account for smoothing of the contours in Figs. 6 and 8. Near-vertical hatches represent schematic columnar joints in the basalt. Those in bold are constrained by field measured flow surface attitudes, and the remainder are inferred. See cross-section locations on Fig. 6 (a–a') and Fig. 8 (b–b'), and photograph in Fig. 5b.
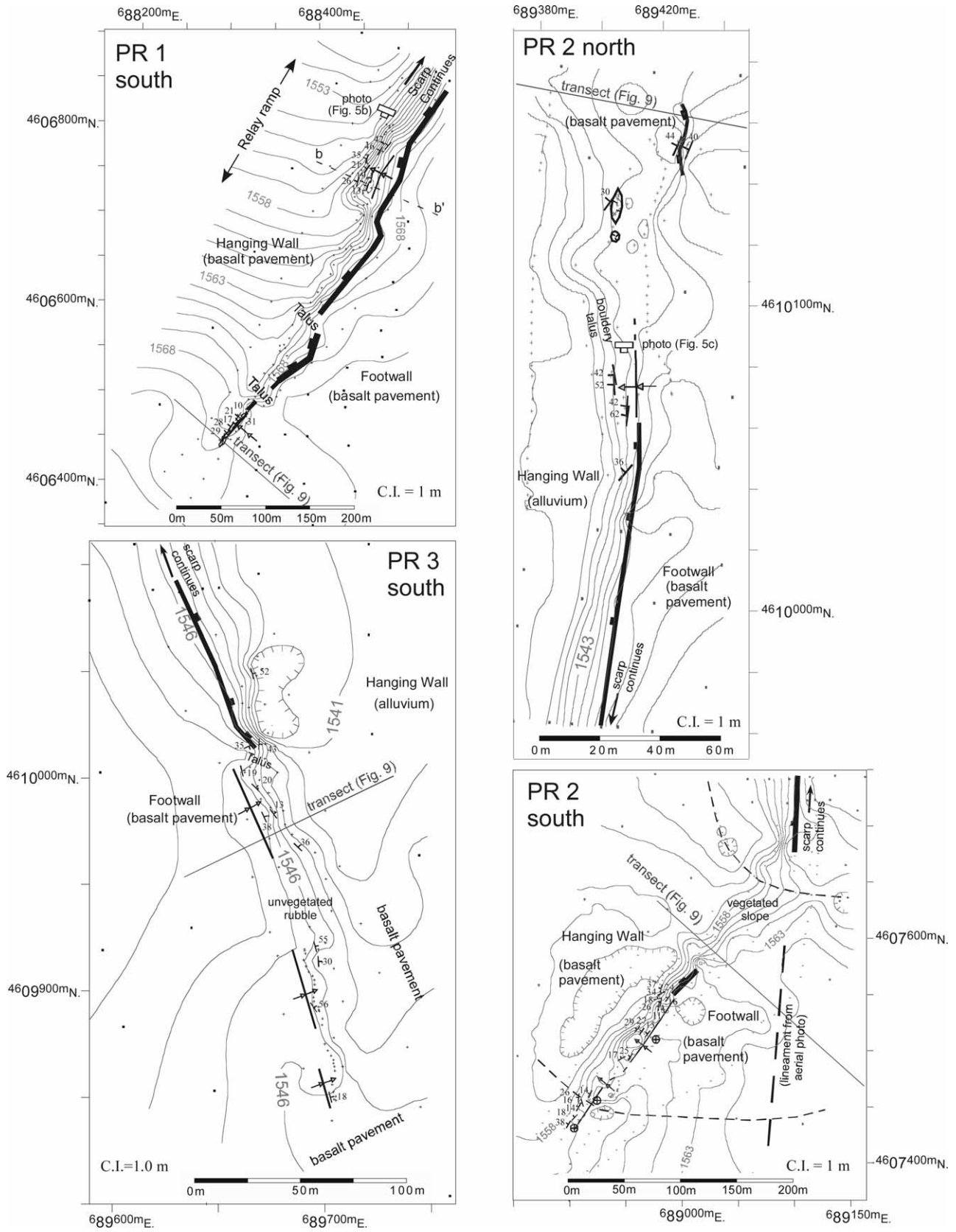
Fig. 8. Structure maps of four fault terminations. See Fig. 3b for location. Symbols as in Fig. 6.

of the fault in this section is organized in a left-stepping array. Near the southern tip of the fault, where the scarp becomes gradually lower, unvegetated talus slopes become increasingly abundant as breaks in the otherwise continuous cliff. South of the cliff-defined sections of the scarp, topographic relief remains, defined by a monocline no more than 2 m in amplitude. There is a 20-m-long fissure along the axis of the monocline with ∼5 m of opening. In regions where the basalt is exposed, it appears coherent and the surface dips moderately to the northwest.

Near the north end of the limits of the detailed survey, a large tilted block of intact basalt similar to the one near the center of PVF crops out (Figs. 5b, 7b and 8). Flow surfaces on the block are well exposed over a large area. They generally strike parallel to the fault trace and dip moderately to the northwest. The structure is located along a prominent left step in the fault and strike of flow surfaces follows that step, with a difference of ∼30° between the southernmost and northernmost measurements. Again, as with the Porcupine Valley structure, the block is separated from the main scarp by a linear trench ∼10 m wide and ∼4 m above the surrounding hanging wall surface. A cross-section through the block reveals that it forms a broad fold with the top of the scarp (Fig. 7b).

2.2.3. Porcupine Rim 2

Porcupine Rim 2 (PR2) is the next fault segment to the north of PR1 in the right-stepping sequence of Porcupine Rim (Figs. 3 and 8). At the south termination of PR2, a splay of the fault diverges to the southwest. Farther south along strike of the main segment of the fault, there is an obvious lineament on the aerial photo. However, this structure is indistinct on the ground, and the major throw is located on the southwest-striking splay. North of the bend, the fault is clearly marked by a cliff (>2 m height) with a pile of talus at its base. To the south, however, relief is marked by a gentle vegetated slope interrupted by a 40-m-long scarp. South of this scarp, the basalt surface is well-exposed. Along the top of the scarp, surfaces are generally horizontal. West of the top of the scarp, surfaces dip gently to moderately to the northwest with increasing dips towards the northwest in the shape of a monocline. The topographic relief of the structure decreases along strike to the south.

At the north termination of PR2, the scarp defines the eastern boundary of a large basin (Fig. 3). The hanging wall surface, like most of the faults examined, is buried in alluvial sediments up to the very tip of the fault trace. In the case of this tip, the end of a cliff-defined scarp coincides roughly with the northern limit of alluvial sediments. Beyond this point, offset grades into a gently sloping hill with the character of bouldery talus. Along this section of the fault, the basalt surface is exposed and dips moderately to the west, striking nearly north (Figs. 5c and 8). North of the scarp, a small circular depression and a 15-m-long fissure with a depth of <1 m occur along strike. Farther north, a long sinuous scarp 1 m in height occurs to the east of the main fault trace. Where it is not degraded, the basalt surface along this feature dips moderately to the west, striking parallel to its trace.

2.2.4. Porcupine Rim 3

Porcupine Rim 3 (PR3) is a small antithetic fault with about 10 m of throw (Fig. 3). It is well defined by a sharp cliff with gradually diminishing relief toward the tips. The basalt surface is exposed in both the footwall and hanging wall, thus the mapped fault tip is both well preserved and well exposed.

In the section of the fault surveyed, the footwall elevation remains fairly constant, whereas the hanging wall elevation changes (Fig. 8). The cliff section of the scarp is sharp and has little to no rubble at its base. In the near-tip region, the basalt is highly vesicular and there appear to be ropy flow surfaces preserved in a number of locations. To the south, the cliff grades into a linear row of unvegetated basalt boulders. There are several locations, however, where the basalt appears intact and is folded into a monocline that dips gently to moderately to the east, striking parallel to the fault trace.

2.3. Topographic transects of near-tip regions

Transects of surface topography at sub-centimeter resolution were acquired using an electronic distance meter and theodolite (total station). Fault-perpendicular transects across the near-tip regions were recorded for six tips, in order to precisely document the shape of the subtly deformed surface (Fig. 9). The fault tip is defined here as the point where the cliff-defined section of the scarp terminates. The transects cross the scarp at 10% of the fault half-length (as expressed at the surface) beyond the fault tip. This value was chosen because it is far enough from the fault tip to be out of the rubble and into intact basalt and because it is still within the region where folding is expressed as a moderate tilting of the basalt surface along strike of the fault.

Transects consistently show nearly flat slopes in the hanging wall with an abrupt increase in slope at the scarp. Transects PR1n and PR1s show slight decreases in hanging wall elevation adjacent to the scarp. These are the only two transects where the hanging wall is not buried in alluvium at the location of the transect. In the footwall, there are two distinct patterns of deformation. PR1s, PR2s, and PR2n show broad anticlinal folding with the crest of the fold between 10 and 15% of fault half-length from the scarp. Amplitudes range from 7 to 36% of the maximum scarp relief. PVFn, PR1s, and PR3s do not crest before intersecting adjacent faults and show varying slopes. Those tips that show broad folds are on rear segments in their respective overlap zones (PR1s and PR2s). PR2n is the front segment in the overlap zone, but there is an antithetic fault (PR3) between the two. PVFn should be sufficiently isolated to produce a broad fold, but there is a large volcanic vent to the north that complicates the topography (Fig. 3b). Topography of PR3n is dominated by the influence of the near-by PR2, a much larger scarp.

Fault-parallel transects were recorded along the footwall and hanging wall of seven scarp terminations along Porcupine Rim. The hanging wall transect was subtracted from the footwall transect in order to profile the surface displacement in
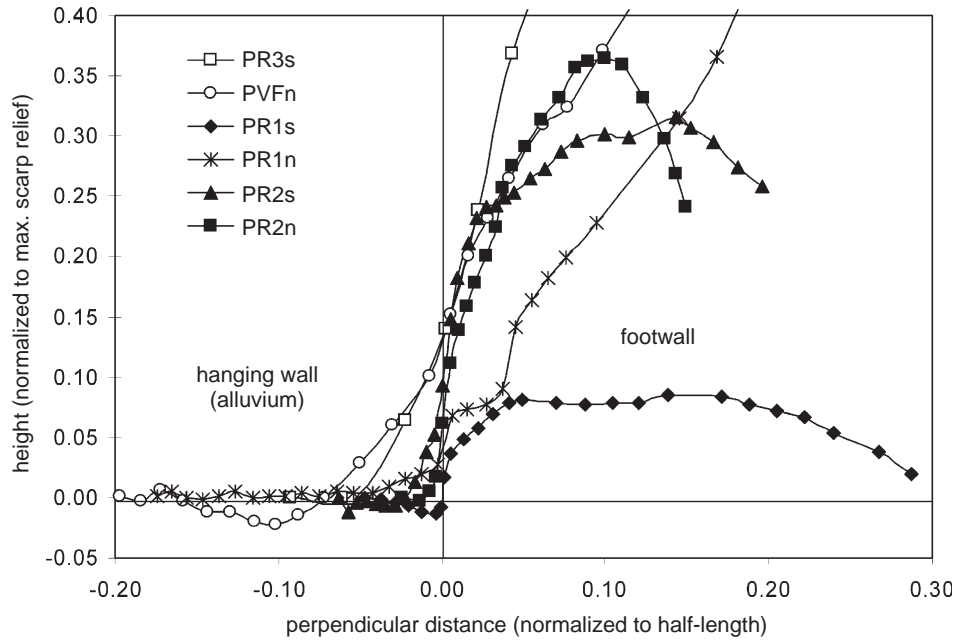
Fig. 9. Topographic transects across the near-tip regions of scarps in the Porcupine Rim region. Elevations were measured by total station and are relative to the hanging wall. Measurement error falls within symbol size. Transects are perpendicular to fault strike and cross the scarp at 10% of the scarp half-length beyond the termination of the cliff-defined section of the scarp. The origin gives the position of the fault scarp, projected along strike. See Fig. 3 for fault locations and Figs. 6 and 8 for transect locations.

the near-tip regions (Fig. 10). The profiles cover 10–25% of the scarp length. In most cases, the hanging wall is buried in alluvium, so the transects represent profiles of minimum surface displacement. The observed profiles are plotted along with idealized footwall profiles generated by elliptical, linear, and bell-shaped slip distributions. The observed profiles fall between the elliptical and linear distributions, closer to the elliptical distribution near the tips, and falling toward the linear

distribution close to the centers of the scarps. Near several of the tips, basalt is exposed in both the footwall and the hanging wall, so it can be assumed that the profiles represent accurate estimates of fault slip. Closer to the fault centers, the values are progressively underestimated as a product of the presumably thickening alluvial wedge that covers the hanging wall. This suggests that slip distributions are most likely elliptical for these faults.
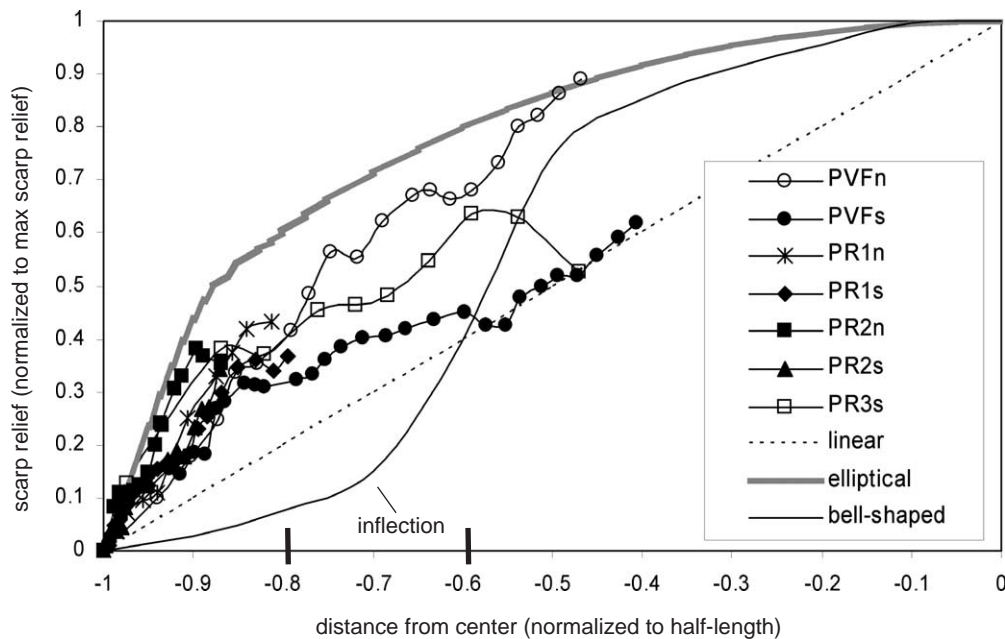

Fig. 10. Observation of along strike distributions of scarp relief compared with idealized footwall relief. Bold black lines represent the range of inflection points observed for faults with bell-shaped slip distributions (Cowie and Scholz, 1992b). Field observations most closely resemble the elliptical distribution. Measurement error falls within symbol size.

2.4. Summary of observations

Fault scarps in this portion of the Modoc Plateau typically have greatest vertical offset near their centers tapering steeply at the tips. The footwalls of observed faults also show a fairly consistent form perpendicular to strike. The maximum footwall elevation is generally back from the scarp (up to 300 m) and diminishes gradually into the footwall. The footwall surfaces observed are a rubbley basalt pavement with sparse vegetation while the hanging walls are generally covered in alluvial sediments.

Along-strike variations in scarp character are fundamental to this study (Fig. 11a). Near the centers, the scarps are defined by a vertical cliff with a talus pile at its base (Fig. 5a). Of the scarps examined, talus piles are generally less than $\sim 1/2$ the height of the scarp. In the near-tip regions, scarp configuration changes to moderately- to gently-sloping rubble slopes. The six near-tip regions examined show tilted flow surfaces (where exposed) striking parallel to scarp trace and dipping gently to moderately towards the hanging wall. The dipping flow surfaces are generally parallel to the topographic slope that they occupy, implying that the observed topography is controlled by the tilted basalt (Fig. 5c). The overall shape of the deformation in the near-tip regions can best be described as a monocline or highly asymmetric anticline with decreasing amplitude beyond the tip (Fig. 11).

Other structures that occur in conjunction with normal faults on the Modoc Plateau include fissures along the crests of near-tip folds and isolated monoclines in the hanging wall. Fissures are preserved in the near-tip regions of three faults: PVFs (Fig. 6), PR1s and PR2n (Fig. 8). Their long axes parallel fault traces and they occur near the end of the zone of fault-related deformation. We posit that these structures are the expression of small amounts of extension at the surface in response to folding.

Isolated monoclines occur in two locations, near the center of the Porcupine Valley Fault (Figs. 6 and 7a) and near the south tip of PR1 (Figs. 5b, 7b and 8). In both cases, the monocline has a slightly curved axis (convex toward the hanging wall) parallel to a linear oblique step in the fault trace. Between the monocline and the scarp there is a separation of 10–15 m. The separation may represent a more well-developed stage of the fissures described above. The isolated monoclines are located in regions of greater offset, so presumably represent a later stage of structural development than features in the tip regions. The location of the monoclines in conjunction with fault step-overs implies that their preservation may be related to fault linkage.
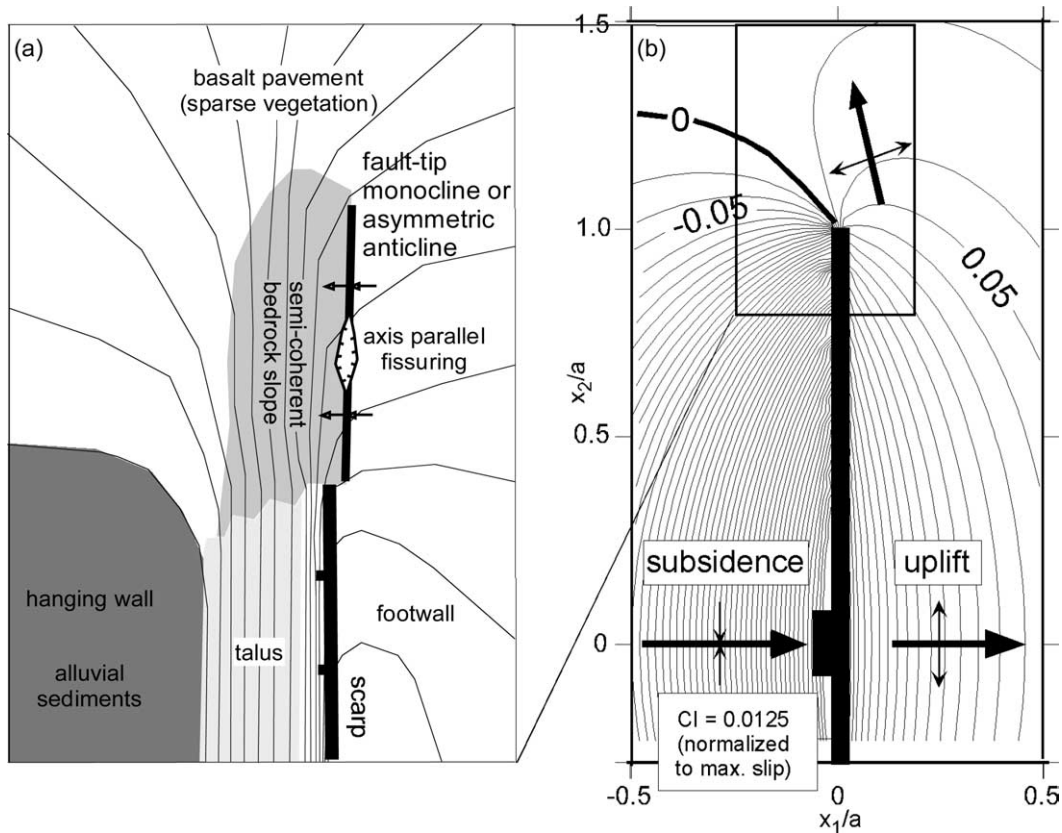

Fig. 11. (a) Idealized contour map of a typical near-tip region of a scarp in the study area. Transition area from cliff-defined scarp to folded rubble slope is gradational and commonly difficult to constrain. (b) Contour plot of vertical displacement at the surface produced by dip slip on a simple semicircular fault (elliptical slip distribution). Fault shape and slip distribution modify the pattern slightly, but the primary characteristics do not change. Box shows approximate area of (a).

3. Modeling

3.1. Background

The Earth's crust behaves elastically on short time-scales in reaction to earthquakes, as demonstrated by propagation of seismic waves. As a result, modeling the crust as an elastic material has long been applied to problems of earthquake deformation (Gupta and Scholz, 1998). Fault-related deformation occurs over longer time-scales with greater displacements, and the permanent deformation observed around fault scarps is by its nature not elastic. Additionally, it is generally accepted that a small zone near the tips of normal faults must behave inelastically, to avoid infinite stress at the tips that a purely elastic model predicts (Cowie and Scholz, 1992b). Even so, elastic models have proven to be useful tools for investigation of fault mechanics.

A number of studies have successfully employed elastic models to evaluate stress perturbations around normal faults. These stresses accurately predict the orientation of linkage structures (Crider and Pollard, 1998; Crider, 2001) and joint geometries (Kattenhorn et al., 2000). Elastic models of interacting faults also predict realistic slip distributions on fault surfaces (Willemse et al., 1996; Maerten et al., 1999).

Deformation of the crust around normal faults has also been addressed in an elastic framework. By summing the effects of multiple earthquake events, Crider and Pollard (1998) reproduce a relay ramp between two interacting faults. Willsey et al. (2002) use a similar approach to test planar and listric fault-geometries associated with monoclinal warping of the Nopolo structure, Baja California. Grant and Kattenhorn (2004) compare model displacements with field observations of normal faults in southwest Iceland. They predict the depth at which a dipping normal fault propagating toward the surface will develop a vertical joint attached to its upper tip line. Densmore et al. (2003) use elastic modeling to produce a deformation field around overlapping normal faults. They then apply a landscape evolution model to that deformation field to examine the effects that the two interacting processes have on catchment-fan system development in relay zones.

Gupta and Scholz (1998) use slip measurements as boundary conditions in an elastic model and were able to directly compare the surrounding surface displacements produced by the model with those existing in the field. They found that elastic modeling accurately predicts surface displacement around normal faults. We adopt their approach for this study. The use of displacement boundary conditions delivers a single valued solution to the boundary value problem, even at large (>1%) strains (e.g. Maerten et al., 2001; Savage and Cooke, 2003).

We use the computer code Poly3D (Thomas, 1993) to test the mechanical controls on fault-propagation folds. Poly3D employs the boundary element method to make numerical approximations of stress, strain, and displacement near a displacement discontinuity embedded in a linear-elastic half-space.

The assumptions of elasticity theory that are inherent to Poly3D include: (1) the fault is embedded in a homogenous and isotropic material that deforms linearly in response to an applied stress, (2) when that stress is removed, so is the deformation, and (3) the material does not contain any voids or fractures besides the fault. Normal faults on the Modoc Plateau cut highly jointed and layered basalts that clearly contain voids and fractures, are not homogeneous, may or may not be isotropic, and show permanent deformation. Poly3D models a continuum, where strain is distributed continuously throughout the solid. From field observations, it is apparent that the strain is localized on joints and is not distributed through the columns, as grain-scale deformation is not observed. We posit an elastic-plastic (spring-block) rheology for these rocks, where the initial deformation response (and therefore the shape of folds) is governed by elastic behavior, and the folds are made permanent by frictional sliding on joints and other fractures within the rock. Thus, we expect the simplified model rheology to capture the first-order forms of folds generated by faulting.

3.2. Methods

By varying Poisson's ratio, fault shape, slip distribution on the fault, fault dip, and including the effects of interacting faults, we attempt to assess the mechanical controls on fault-propagation folds and make some comparison with those folds observed in the field. In each case, the problem is addressed in a half-space framework, remote strains are zero, and fault slip is prescribed by down-dip displacements (b_1) on fracture elements (Fig. 12). Additionally, element-normal displacement (b_3) is set to zero to keep the fault from opening and horizontal traction (t_2) is set to zero to allow opposing sides of the fault to move laterally relative to one another in response to vertical movement. Unless otherwise stated, we chose to use a Poisson's ratio of 0.25 and a shear modulus G of 30 GPa—reasonable values for intact basalt (Middleton and Wilcock, 1994, p. 419)—and fault dip of 60°. Calculations of displacement in the x_1, x_2, and x_3 directions were made at an array of tightly spaced points around the fault. Vertical displacements are either positive (uplift) or negative (subsidence) relative to an absolute datum that represents the original free surface of the modeled half-space before fault slip has been applied. The resulting folds are most strictly named fault-arrest folds (e.g. Johnson and Johnson, 2002a), as the fault is not allowed to grow during the slip increment. To allow comparison of fold shapes between faults of varying lengths, heights, and throws, displacements are normalized to the maximum slip on the fault at the surface or to fault height, and horizontal distances are normalized to fault half-length at the surface. Topography in both the footwall and the hanging wall is modeled, but given that the hanging wall is commonly obscured by alluvium, the differences in footwall profiles are more important for comparison with field data. We discuss how the differences in model profiles translate to a real distance that could be compared with field data.
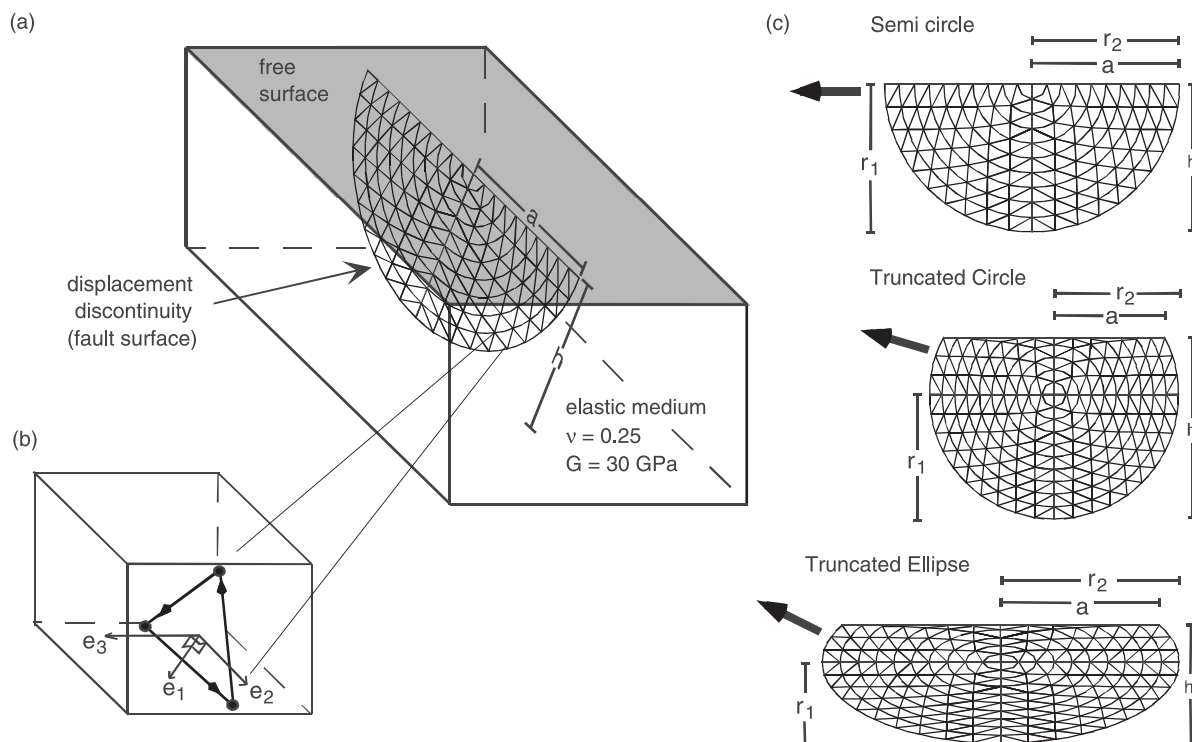
Fig. 12. (a) Elliptical displacement-discontinuity of half-length a and height h, embedded in a semi-infinite elastic half-space with Poisson's ratio ν and shear modulus G. We use a to designate the fault half-length at the free surface and r_i to indicate semi-axes of the ellipse. (b) The displacement discontinuity is discretized into triangular elements of constant traction (t_i) and/or displacement (b_i) in each of three directions defined by e_i. Each fault is discretized into 10 rings of triangular elements. Boundary conditions are varied by ring to approximate realistic slip distributions on the fault surface. (c) Modeled fault shapes. For the semicircle, $r_1/r_2 = 1$, and $a = r_2$. For the truncated circle, $r_1/r_2 = 1$, and $a < r_2$. For the truncated ellipse, $r_1/r_2 = 2$, and $a < r_2$. Bold arrow represents expected propagation direction at or near the surface.

3.3. Results

3.3.1. Slip distribution

We tested three commonly proposed normal fault slip-distributions; linear, elliptical, and bell-shaped (Fig. 10), to evaluate the effect of each on fold form. In each case, the slip is at a maximum at the center of the fault and decreases to zero at the tips. Elliptical distributions are predicted by purely elastic models driven by remote stress and show large displacements near the tips decreasing very rapidly to zero (Jaeger and Cook, 1979). Bell-shaped distributions are predicted by cohesive end zone models (Cowie and Scholz, 1992b) and near the tips show small displacements tapering to zero. The cohesive end zone is marked by a concave up inflection in the slip profile. Cohesive end zones are typically 20–40% of the fault half-length for faults with bell-shaped slip distributions (Cowie and Scholz, 1992b). We chose a cohesive end zone of 30% of the fault half-length for comparison with field data. Linear distributions are the simplest way to decrease slip toward the tips. Such 'triangular' shapes are observed in earthquake slip distributions (Manighetti et al., 2003) and some faults (e.g. Dawers et al., 1993). By using a simple half-ellipse fault shape and varying only the slip distributions, we can make some general statements about the effect of varying slip distribution on deformation beyond the tip line of a simple normal fault.

For a simple semi-circular fault with $a = 1$ and maximum slip $= 0.015a$ (comparable with field observations of maximum

relief on Modoc Plateau scarps), varying slip distributions produce folds of varying amplitudes beyond the tip lines (Fig. 13). In each case, along a fault-perpendicular transect $0.1a$ beyond the fault tip, the maximum vertical displacement is offset from the longitudinal projection of the fault by $\sim 0.15a$ in the footwall and $\sim 0.3a$ in the hanging wall. Elliptical and linear distributions produce an anticline/syncline pair with uplift in the footwall and subsidence in the hanging
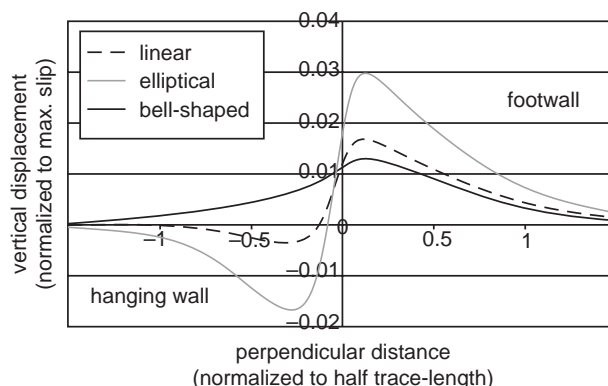

Fig. 13. Model results for faults of varying slip distribution. Distribution of vertical displacement is measured at the free surface of the modeled half-space along a fault-perpendicular transect at 10% of the fault half-trace-length beyond the fault tip. Fold amplitude increases from bell-shaped to linear to elliptical, and bell-shaped distributions produce only uplift at this position beyond the fault tip.

wall, while bell-shaped distribution produces an anticlinal fold with uplift of both the footwall and the hanging wall. Folds decrease in amplitude from elliptical to linear to bell-shaped distributions. This corresponds to a decrease in the amount of fault slip near the tips, where more slip produces higher amplitude folds. For a fault with $a = 1$ km, the difference in amplitude between the elliptical and linear distributions amounts to ~60 cm, a difference that should be recognizable in field data. The difference in amplitude between the bell-shaped and linear distributions, however, amounts to less than 10 cm. This is within the accuracy of a total station survey, but due to the uneven basalt surface, is probably not resolvable.

It is evident that the relative amount of hanging wall subsidence decreases from elliptical to linear to bell-shaped distributions, and that the shapes of the profiles are nearly identical in the footwall. Because a bell-shaped distribution produces no hanging-wall subsidence, alluvial filling of the hanging wall is expected in near-tip regions of faults with elliptical and linear distributions, but not those with a bell-shaped distribution at the surface.

3.3.2. Fault shape

We test three reasonable fault shapes for isolated normal faults (Fig. 12c): a semicircle, a truncated circle, and a truncated ellipse. If we assume that fault propagation direction is perpendicular to the fault tip-line, a semicircular fault will propagate purely laterally at the surface. Embedding a circle deeper than the bisection line will add a component of vertical propagation. The semicircle that we model is a bisected circle (aspect ratio = 1) that intersects with the free surface at its maximum horizontal length, so half-length (a) is equal to the radius (r) of the circle. The truncated circle intersects the free surface so that $a = 0.9r$, leaving the maximum fault length buried below the surface as a blind fault. This value was chosen based on the lateral extent of deformation beyond the tip of faults in the study area, assuming that the observed deformation is a consequence of vertical fault propagation. The truncated ellipse is similar to the truncated circle but with an aspect ratio of 2, which brings the section of the fault that is blind nearer to the surface and steepens the propagation direction at the surface (Fig. 12c).

We test each fault shape with elliptical, linear, and bell-shaped slip distributions. To isolate the effects of varying shape, we chose to hold fault area constant and normalize displacement to fault height. Fault size greatly affects the amplitude of deformation, but not the shape of the fold, which is of interest here. Perpendicular cross-sections at $0.1a$ beyond the surface terminations of the three fault shapes reveal distinct patterns of warping at the surface (Fig. 14). The truncated circle shows a similar shape for each slip distribution: high amplitude anticline/syncline pairs with more hanging wall subsidence than footwall uplift. The fold is increasingly tighter (mainly in the hanging wall) from bell-shaped to linear to elliptical slip. For a fault with $a = 1$ km, the fold crests vary in position up to 60 m, a difference that can be recognized in the field. The truncated ellipse consistently shows medium amplitude folds while the semicircle produces the lowest-

amplitude folds. This difference in amplitude, however, amounts to less than 20 cm for a fault with $a = 1$ km, a difference that would be difficult to resolve. The semicircle uplifts the surface into a gentle symmetric anticline for bell-shaped slip (Fig. 14c) and produces only minute amounts of subsidence for linear slip (Fig. 14b). The truncated circle and the truncated ellipse consistently produce anticline/syncline pairs, though for bell-shaped and linear slip on the truncated ellipse there is hanging wall uplift in the form of a hanging wall bulge (Fig. 14b and c). The buried tip lines of the truncated circle and truncated ellipse extend $0.1a$ beyond the surface trace, coinciding with the model transect and apparently generating larger folds.
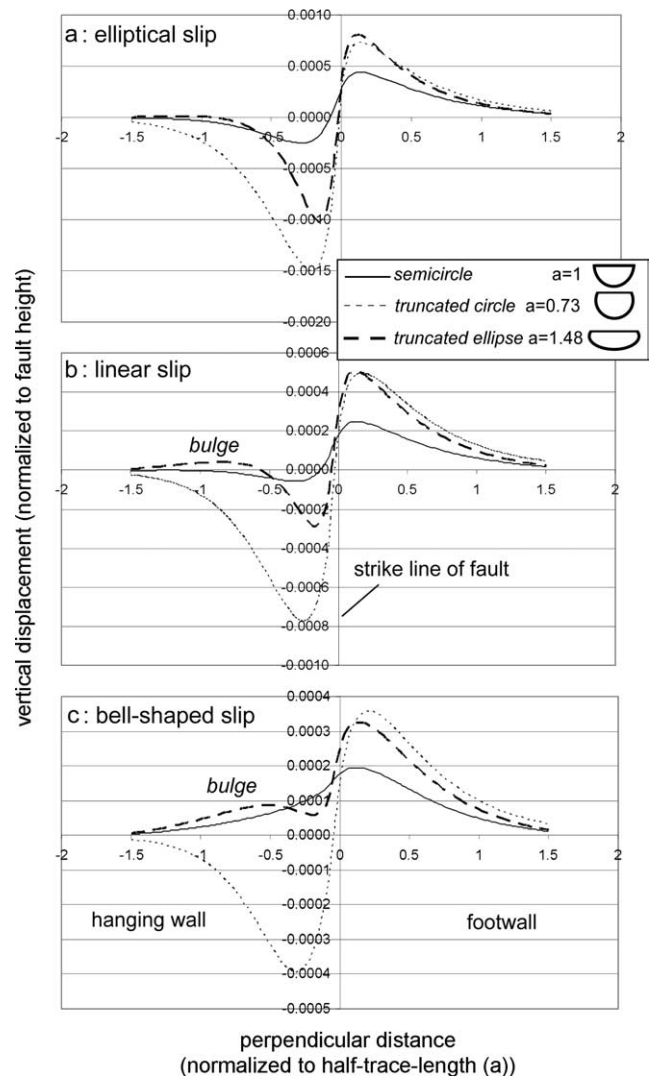

Fig. 14. Comparison of folds produced by faults of varying shape. Distribution of vertical displacement was measured at the free surface of the modeled half-space along a fault-perpendicular transect at 10% of the fault half-trace-length beyond the fault tip. Fault shapes and values for half-trace-length, a, are shown in the inset. Area of the fault is held constant among trials. Three slip distributions were applied to each fault shape: elliptical (a), linear (b), and bell-shaped (c). Note that the vertical scale differs in each graph. Varying slip distribution has a greater influence on the semicircle and truncated ellipse than on the truncated circle. The truncated ellipse shows uplift (bulge) in the hanging wall with linear and bell-shaped slip.

3.3.3. Interacting faults

We attempted to survey isolated fault tips on the Modoc Plateau. This proved difficult. As a result, the majority of the tips that were examined, though not connected to other structures at the surface, are subject to the mechanical influence of neighboring faults. To account for this influence, we modeled fault pairs of varying shape and slip distribution in a right-stepping arrangement. The pairs were given an overlap of $0.5a$ and a separation of $0.2a$ (Fig. 15) based on the average configuration of relay pairs in the Porcupine Rim structure. It is possible that the faults we observed are splays off a larger fault connected at depth. If this is the case, our model underestimates the fault height and thus also the likely extent of folding around the faults.

For two overlapping faults, folding produced ahead of the tip of either fault is greatly overwhelmed by the influence of deformation due to the neighboring fault. In order for folds to be produced, the deformation ahead of the fault must be great enough to exert an influence on the deformation field surrounding the neighbor. As a result, profiles of folding ahead of both the front and back segments reveal that elliptical slip distributions produce the highest amplitude folds (Fig. 16). This is in agreement with the general observation that elliptical slip distributions have more slip near the tip and thus higher displacements in the surrounding material. The profiles also suggest that folds in relay zones are produced more easily by fault shapes with stronger components of vertical propagation (truncated circle and truncated ellipse). The gentle anticlines that are produced ahead of isolated semicircles are overwhelmed by the displacement produced by the neighboring fault. Finally, modeling suggests that high amplitude folds are more likely to form ahead of the rear fault in a sequence, rather than the front fault. The rear fault is competing with uplift (positive displacement) from its neighbor, whereas the front fault is competing with subsidence (negative displacements). For dipping normal faults, negative displacements are much greater than positive displacements with an increasing disparity
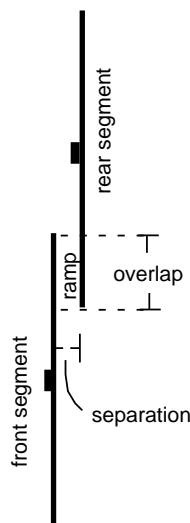
closer to the center of the fault. Thus, folds ahead of rear segments may be preserved due to summation of uplifts in the footwall, whereas anticlines ahead of front segments are cancelled by subsidence in the hanging wall of the rear segment.

3.3.4. Elastic properties

Poisson's ratio describes how strain in x_1 is transferred to x_2 and x_3. Lower values of Poisson's ratio correspond to materials that do not transfer strain as effectively. For fractured material, like jointed basalt columns, communication of strain from one direction to another may be reduced, effectively lowering Poisson's ratio. We tested the effect of lowering Poisson's ratio from 0.25 to 0.05 on a simple semicircular fault with linear, elliptical, and bell-shaped slip distributions (Fig. 17). In each of the three cases, folding became tighter, uplift of the footwall became greater, and hanging wall subsidence near the fault trace became less. The difference in amplitude is on the order of 10 cm for a fault with $a = 1$ km. This difference is not resolvable for faults on the scale of those examined on the Modoc Plateau. The difference in crest position, however, is on the order of 100 m and should be resolvable in field data.

3.3.5. Fault dip

The modeling described above was performed under the assumption that fault dip is 60°. Here, we evaluate the effects of varying fault dip and whether these effects are resolvable in the field. For a simple half circle with an elliptical slip distribution, fold amplitude increases with increasing dip and fold tightness (in the footwall) decreases with increasing dip (Fig. 18; cf. Willsey et al., 2002, fig. 9). It is also interesting to note that the degree of asymmetry between footwall uplift and hanging wall subsidence decreases with increasing dip and is symmetrical for a vertical fault. The variation in shape and amplitude for the profiles is greatest in the hanging wall. The hanging wall is covered by alluvium for the faults that we surveyed, so with the exception of a 45° dipping fault, which predicts uplift only, these distinctions cannot be resolved in the field. The variation in footwall fold amplitude for a fault with a half-length of 1 km (typical of faults examined on the Modoc Plateau) is on the order of 10 cm or less. Although this difference can be resolved with a total station, the basalt surface is too uneven for this variation to be meaningful. However, the position of the anticline crest in the footwall migrates ~ 60 m for a 15° change in fault dip. If this effect can be isolated, it should show up in field data.

4. Field-model comparison

Fault-perpendicular topographic transects across near-tip regions of normal fault scarps on the Modoc Plateau (Fig. 9) reveal that the footwall is commonly folded into a broad asymmetric anticline with its crest displaced between $0.1a$ and $0.15a$ normal to the trace of the scarp. Folding occurs ahead of the fault tip, presumably as the result of fault propagation. The folds are expressed topographically and by tilting of basalt columns along strike of the scarp. The axis of folding is parallel

Fig. 15. Terminology used for overlapping fault pairs (modified from Crider and Pollard, 1998).
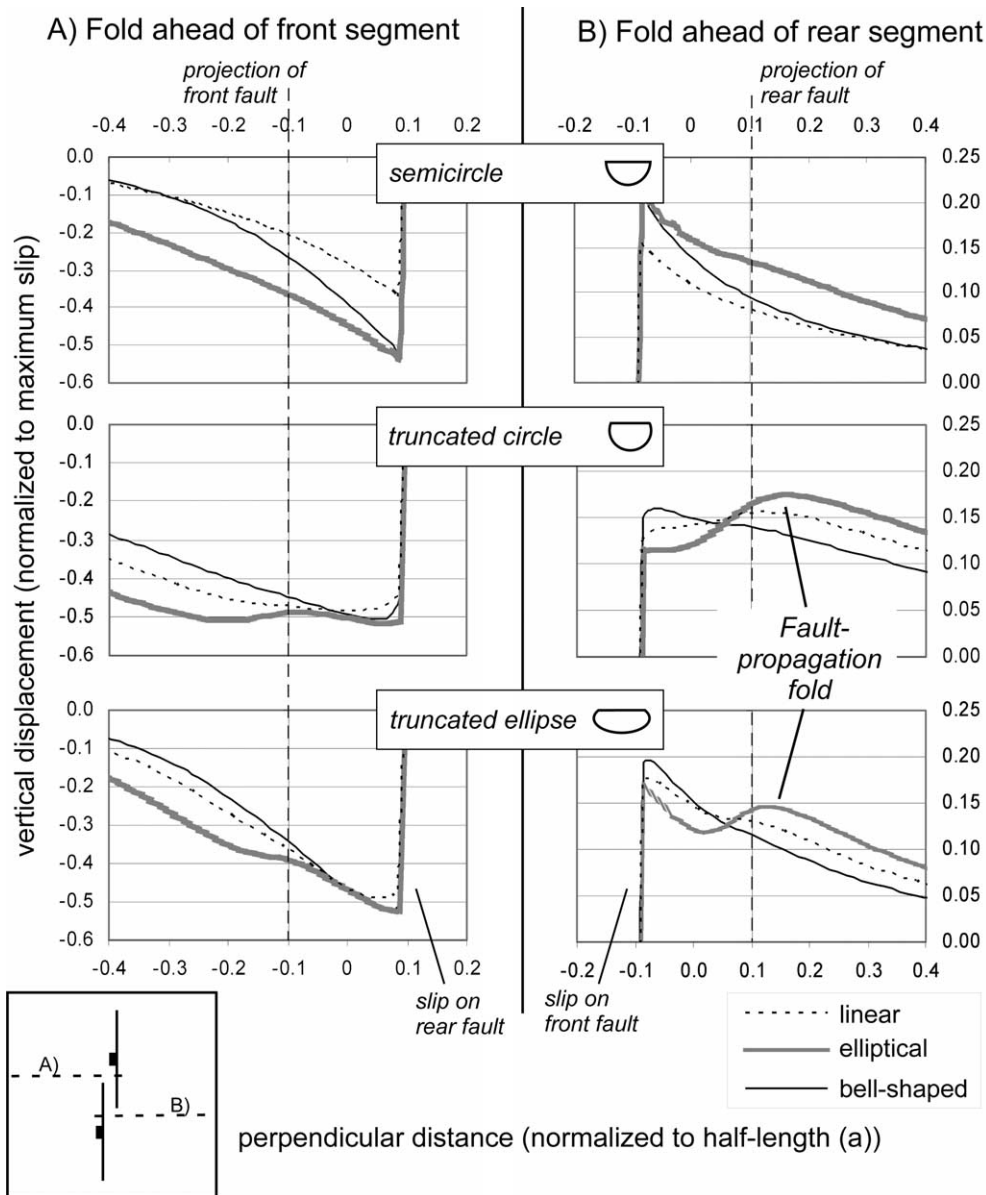
Fig. 16. Model results for interacting faults of varying shape and slip distribution. Distribution of vertical displacement is measured at the surface of the modeled half-space along a fault-perpendicular transect for overlapping faults of variable shape and slip distribution. Both faults in each pair have the same shape, size, and slip distribution. Column A shows profiles of surface displacement at $0.1a$ ahead of the front fault. Column B shows profiles displacement at $0.1a$ ahead of the rear fault of the same fault pair. Inset shows approximate location of profiles.

to fault strike and fold amplitude decreases with distance from the fault.

Linear-elastic boundary element modeling of simple isolated normal faults allows examination of the mechanical controls on fault-propagation folds. Slip distribution affects primarily the amplitude of folding. Elliptical slip distribution produces relatively high amplitude folds, while bell-shaped slip distribution produces low amplitude folds. Fault shape, which controls inferred propagation direction, is shown to produce varied patterns of surface warping in the near-tip regions, especially in the hanging wall. The primary difference that is observed is in the amount of hanging wall subsidence, relative to footwall uplift. Vertical fault-propagation folds (truncated circle and truncated ellipse fault) show more relative hanging

wall subsidence than lateral fault-propagation folds. For interacting faults in a relay zone, the model predicts that fault propagation folds will be visible only for faults with elliptical slip distributions. Folds on interacting faults are similar in amplitude to those on isolated faults, but are consistently tighter and more symmetrical. Finally lowering Poisson's ratio appears to increase fold amplitude and tightness, and increasing dip increases amplitude but decreases tightness.

Modeling normal faults as discontinuities in a linear elastic half space accurately reproduces the first-order features of normal fault-related deformation in the study area. Uplift of the footwall into an open plunging anticline with its axis perpendicular to fault strike (a displacement-gradient fold) is seen both in the field and in model simulations (Fig. 11b).
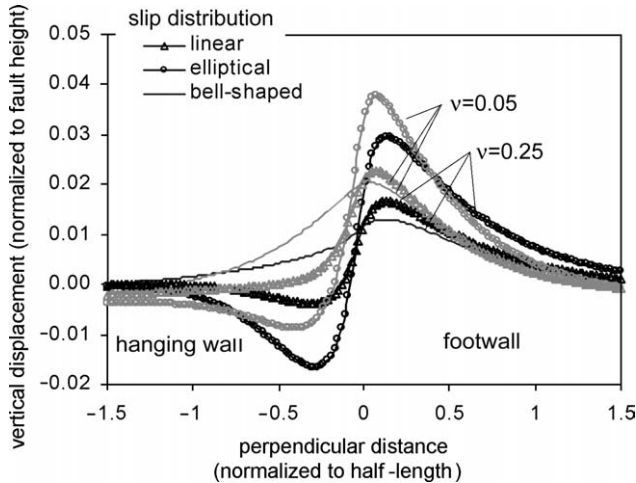
Fig. 17. Model results for faults in material of varying Poisson's ratio. Distribution of vertical displacement measured at the free surface of the modeled half-space along fault-perpendicular transects at $0.01a$ beyond the fault tip for linear, elliptical, and bell-shaped slip distributions on a semicircular fault. In each case, fold amplitude and tightness increase with a lower value of Poison's ratio.

In the model framework, a fault-perpendicular syncline is predicted in the hanging wall. Presumably, these are present in the field as well, but are filled with alluvial sediments, making them difficult to observe. It is also interesting to note that elastic modeling predicts that hanging wall subsidence will be two and a half times greater than footwall uplift for a fault dipping 60°. This implies that field measurements of scarp relief (Fig. 10) may significantly underestimate the true slip, more so near the fault centers. In the near-tip regions, elastic modeling predicts low amplitude folding ahead of the fault (Fig. 11b). The axes of the folds are sub-parallel to fault strike and offset slightly to the footwall side of the fault. Folding is present at all the fault tips that were mapped, also offset to the footwall.
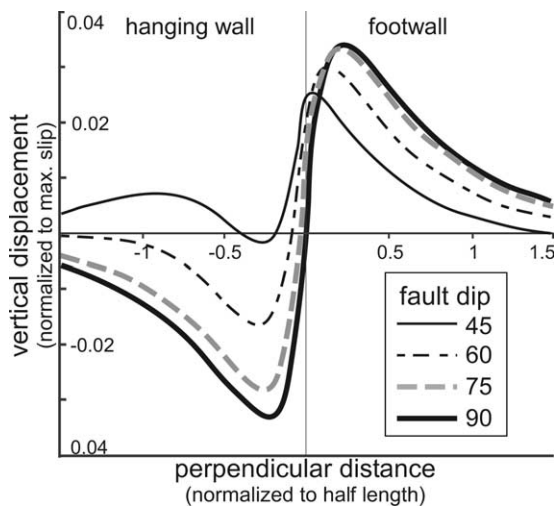

Fig. 18. Modeled folds for faults (semicircle, elliptical slip) of different dip. Displacement at the free surface of the modeled half-space along a fault-perpendicular transect at $0.1a$ beyond the fault tip. Fold amplitude increases with increasing dip and fold tightness in the footwall decreases with increasing dip.

The main goal of this study is to use field observations in conjunction with elastic modeling to understand some fundamental controls on fault-propagation folding. In particular, what is the role of propagation direction (fault shape), and can one scenario be distinguished from another on the basis of observed surface deformation? We compare field observations directly with modeled results via topographic transects $0.1a$ beyond the exposed fault tip. To compare faults of different lengths and throws, we normalize horizontal position to fault half-length (a) and vertical displacement to maximum footwall uplift. Fault half-length is easily obtained from real and modeled faults. Maximum footwall uplift is easily obtained for modeled faults, but requires a degree of interpretation for real faults. We assume that the hanging wall is entirely filled with sediments, so that scarp relief expresses uplift only, and maximum scarp height is equal to the maximum footwall uplift.

We surveyed two topographic transects from rear segments in relay pairs, PR1s and PR2s. The profiles most closely resemble the modeled truncated circle with elliptical slip distribution (Fig. 19), implying that faults in Porcupine Rim are not simple semicircles and that there are portions of the faults that are blind. The amplitude of the PR2s fold varies considerably from the modeled folds. This variation may be considerably exaggerated as a result of normalization problems or difficulty in defining the precise location of the fault tip in the field. If the transect is actually positioned at $0.05a$ (an error of 75 m in the field) from the fault tip, the fold has higher amplitude and matches, very nearly, the profile for a truncated circle with elliptical slip.

The topographic transect of PR2n, though positioned in front of a large fault segment as a relay pair (Fig. 3), is considered here to be sufficiently isolated from the influence of neighboring faults that it can be compared with model
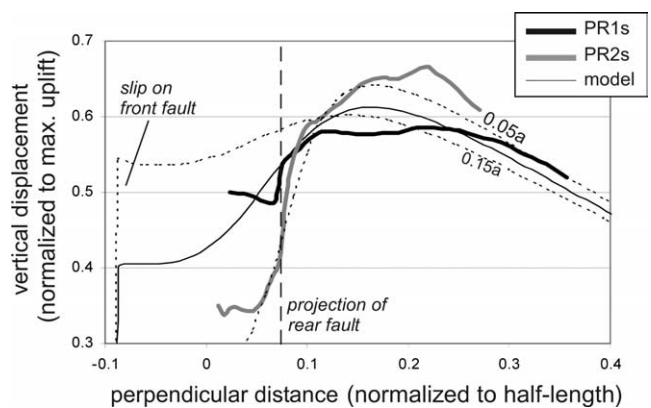

Fig. 19. Comparison of field transects to model transects for rear segment in overlapping fault pairs. Transects are fault-perpendicular and located $0.1a$ beyond the fault tip. Model is a truncated circle with elliptical slip distribution, $n=0.25$, $G=30$ GPa, dip$=60°$, and maximum slip on the faults is $0.015a$. Dashed lines represent variation from shifting the model transect laterally by $\pm0.05a$. Horizontal position of field data is constrained by fault location, but vertical position is unconstrained. Field data were matched vertically to model output as closely as possible. Error in topographic measurement is smaller than line width. Normalized position of front fault for field examples is -0.14 for PR1s and -0.16 for PR2s.
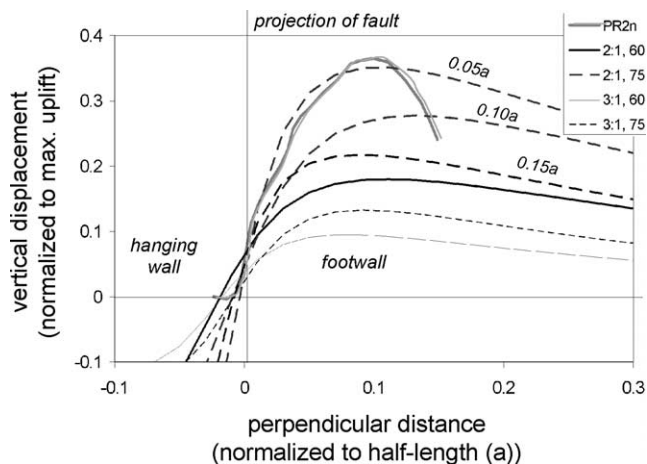
Fig. 20. Comparison of PR2n transect to model results for elliptical slip on truncated ellipses with variable aspect ratio (2:1 or 3:1) and fault dip (60° or 75°). Transects are fault perpendicular and located 0.1a beyond the fault tip, except as noted. Error in topographic measurement is smaller than line width. Match is achieved for fold amplitude and position of the anticline crest.

results for a single isolated fault. The amplitude of folding associated with this fault is much higher than modeled amplitudes, but the position of the fold crest ($\sim 0.1a$) is nearly identical to modeled crests for both semicircles and truncated ellipses (Fig. 20). The pattern of footwall deformation most closely resembles that for a truncated ellipse with elliptical slip.

In an attempt to better match the PR2n transect, we make simple variations on the truncated ellipse fault with elliptical slip. Lowering Poisson's ratio was shown to increase amplitude in the previous section. However, it was also shown to shift the crest of the fold toward the fault, which is not desirable in this case. Instead we test the effects of increasing the aspect ratio of the fault (steepening propagation direction), increasing the fault dip (to increase footwall amplitude and decrease tightness), and looking at transects that are laterally closer to the modeled fault tip (to account for errors in locating the fault tip and defining its half-length in the field). Increasing the aspect ratio from 2:1 to 3:1 for a truncated ellipse lowers the amplitude of footwall deformation. This is not desirable for producing a better match here. Increasing the dip of a 2:1 truncated ellipse to 75°, however, brings the model profile much closer to the field observations. When the field measurement error is considered, a transect at $0.05a$ beyond the fault tip for a 2:1 truncated ellipse dipping 75° matches the field data very closely from the crest faultward. The most remarkable difference between the modeled deformation and the field observations is in the slope of the footwall behind the fold crest. Modeling predicts a gentle slope, creating an asymmetric fold. In the field, the slope is steep, creating a nearly symmetric anticline. The difference may be attributed to mechanical layering and anisotropy in the basalt versus the modeled homogeneous and isotropic half space (cf. Johnson and Johnson, 2002b), or to topography generated by a neighboring antithetic fault.

5. Discussion

Two interesting conclusions can be drawn from the combination of fieldwork and modeling presented here. First, elastic modeling suggests that fault-propagation folds may be produced ahead of both laterally and vertically propagating normal faults. However, comparison with field observations suggests that such folds, both in relay zones and ahead of isolated tips, are the result of faults with some component of vertical propagation. In three cases, the pattern of deformation in near-tip regions is most closely approximated by truncated-ellipse or truncated-circle fault shapes. In relay zones, a truncated circle with elliptical slip produces the best match and, for isolated tips, a steeply dipping truncated ellipse produces the best match. In no instance was a simple semicircle sufficient to produce the observed deformation.

Second, field data and modeling suggest that slip distributions for normal faults on the Modoc Plateau are elliptical. Observed distributions most closely resemble elliptical slip (Fig. 10), and observed folds are most closely approximated by faults with elliptical slip (Figs. 19 and 20). This validates the use of linear elastic models, which inherently produce elliptical slip distributions, for normal fault problems where surface deformation is of interest.

A number of workers have examined slip distributions on normal faults in other parts of the world with mixed results. Linear slip distributions have been observed along normal fault surfaces in Coal Measures, Britain (Walsh and Watterson, 1987) and on normal fault scarps on the Volcanic Tableland, California (Dawers et al., 1993). Moore and Schultz (1999) observed what they thought resembled bell-shaped slip distributions on normal faults in Canyonlands, Utah. A population of small (centimeter scale) normal faults in the Solite Quarry, Virginia exhibits both elliptical and bell-shaped slip distributions (Schlische et al., 1996). Faults scarps on the Modoc Plateau exhibit elliptical slip distributions. This wide variation in styles of slip on normal faults indicates that either the faults are mechanically different or that there is inconsistency in the measurement of slip distributions (Walsh and Watterson, 1988). Cowie and Scholz (1992a) suggest that displacement distribution can be irregular on a fault surface, resulting in varying slip distributions depending on where the distribution is sampled (i.e. where the fault surface intersects with the Earth's surface). If the point of maximum slip on a fault surface is buried, one might expect to see a linear or elliptical slip distribution even if the distribution at depth is bell-shaped. This agrees with our interpretation that fault tips on the Modoc Plateau are partially buried.

The goal set out at the beginning of this study was to examine the effects that propagation direction, lateral versus vertical, and the fault shapes that those directions imply, have on the production and shape of fault-propagation folds in extensional settings. Previous work has not differentiated between these scenarios (Gawthorpe et al., 1997; Sharp et al., 2000; Willsey et al., 2002). This study shows that, at least on the Modoc Plateau, extensional fault-propagation folds are the result of faults with a component of vertical propagation.

In other words, fault-propagation folds on the Modoc Plateau are rooted in a partially blind normal fault. As the fault accumulates throw, it will propagate laterally and vertically through the overlying fold, forcing growth of the monocline. Peacock and Parfitt (2002) suggest that surface fissures at the crest of monoclines on Kilauea Volcano propagate downward and start accumulating throw as the mechanism of fault growth. We observe similar fissures on the Modoc Plateau but prefer to interpret them as a consequence of fault growth, rather than an initiator. This interpretation is more consistent with Grant and Kattenhorn (2004) who suggest that vertical joints propagate to the surface from a dipping normal fault once the normal fault is in sufficient proximity to the surface (see also Martel and Langley, 2006).

The interpretations in this study are based primarily on the amplitude, tightness, and shape of footwall anticlines observed on the Modoc Plateau. Elastic modeling of dipping normal faults consistently shows that the greatest variation in patterns of deformation occurs in the hanging wall. Future studies of normal fault-related folding would be well-served by focusing on areas where the hanging wall is better exposed or where geophysical techniques are applied to uncover the hanging wall. In addition, mechanical layering and anisotropy, not included in our models, are likely to have a significant influence on fold shape.

Acknowledgements

References

Blakely, R.J., Christiansen, R.L., Guffanti, M., Wells, R.E., Donnelly-Nolan, J.M., Muffler, L.J.P., Clynne, M.A., Smith, J.G., 1997. Gravity anomalies, Quaternary vents, and Quaternary faults in the southern Cascade Range, Oregon and California: implications for arc and backarc evolution. Journal of Geophysical Research 102, 22,513–22,527.

Corfield, S., Sharp, I.R., 2000. Structural style and stratigraphic architecture of fault propagation folding in extensional settings: a seismic example from the Smørbukk area, Halten Terrace, Mid-Norway. Basin Research 12, 329–341.

Cowie, P.A., Scholz, C.H., 1992a. Displacement–length scaling relationship for faults: data synthesis and discussion. Journal of Structural Geology 14, 1149–1156.

Cowie, P.A., Scholz, C.H., 1992b. Physical explanation for the displacement–length relationship of faults using a post-yield fracture mechanics model. Journal of Structural Geology 14, 1133–1148.

Crider, J.G., 2001. Oblique slip and the geometry of normal-fault linkage: mechanics and a case study from the Basin and Range in Oregon. Journal of Structural Geology 23, 1997–2009.

Crider, J.G., Pollard, D.D., 1998. Fault linkage: three-dimensional mechanical interaction between echelon normal faults. Journal of Geophysical Research 103, 24,373–24,391.

Dawers, N.H., Anders, M.H., 1995. Displacement–length scaling and fault linkage. Journal of Structural Geology 17, 607–614.

Dawers, N.H., Anders, M.H., Scholz, C.H., 1993. Growth of normal faults: displacement–length scaling. Geology 21, 1107–1110.

Densmore, A.L., Dawers, N.H., Gupta, S., Allen, P.A., Gilpin, R., 2003. Landscape evolution at extensional relay zones. Journal of Geophysical Research 108, EGT 11-1–EGT 11-15.

Gawthorpe, R.L., Sharp, I.R., Underhill, J.R., Gupta, S., 1997. Linked sequence stratigraphic and structural evolution of propagating normal faults. Geology 25, 795–798.

Gay, T.E., Aune, Q.A., 1958. Geologic Map of California, Olaf P. Jenkins Edition, Alturas Sheet. California Division of Mines and Geology, scale 1:250,000.

Grant, J.V., Kattenhorn, S.A., 2004. Evolution of vertical normal faults at the surface at an extensional plate boundary, southwest Iceland. Journal of Structural Geology 26, 537–557.

Gupta, A., Scholz, C.H., 1998. A model of normal fault interaction based on observation and theory. Journal of Structural Geology 22, 865–879.

Haneberg, W.C., 1992. Drape folding of compressible elastic layers: I. Analytical solutions for vertical uplifts. Journal of Structural Geology 14, 713–721.

Hardy, S., McClay, K., 1999. Kinematic modeling of extensional fault-propagation folding. Journal of Structural Geology 21, 695–702.

Hedel, C.W., 1980. Late-Quaternary movement along the Surprise Valley Fault, with accompanying road log. In: Kramer, C.J. (Ed.), Geologic Guide to the Modoc Plateau and Warner Mountains. Annual Field Trip Guide of the Geological Society of Sacramento, pp. 82–95.

Horsfield, W.T., 1977. An experimental approach to basement-controlled faulting. Geologie en Mijnbouw 56, 363–370.

Jaeger, J.C., Cook, N.G.W., 1979. Fundamentals of Rock Mechanics. Chapman and Hall, London.

Janecke, S.U., Vandenburg, C.J., Blankenau, J.J., 1998. Geometry, mechanisms and significance of extensional folds from examples in the Rocky Mountain Basin and Range province, U.S.A. Journal of Structural Geology 20, 841–856.

Jennings, C.W., 1994. Fault activity map of the California and adjacent areas. California Division of Mines and Geology, Geologic Data Map No. 6, scale 1:750,000.

Johnson, K.M., Johnson, A.M., 2002a. Mechanical models of trishear-like folds. Journal of Structural Geology 24, 277–287.

Johnson, K.M., Johnson, A.M., 2002b. Mechanical analysis of the geometry of forced-folds. Journal of Structural Geology 24, 401–410.

Kattenhorn, S.A., Aydin, A., Pollard, D.D., 2000. Joints at high angles to normal fault strike: an explanation using 3-D numerical models of fault-perturbed stress fields. Journal of Structural Geology 22, 1–23.

Khalil, S.M., McClay, K.R., 2002. Extensional fault-related folding, northwestern Red Sea, Egypt. Journal of Structural Geology 24, 743–762.

Kramer, J.C. (Ed.), 1980. Geologic Guide to the Modoc Plateau and the Warner Mountains. Annual Field Trip Guidebook of the Geological Society of Sacramento, CA.

Maerten, L., Willemse, E.J.M., Pollard, D.D., Rawnsley, K., 1999. Slip distributions on intersecting normal faults. Journal of Structural Geology 21, 259–271.

Maerten, L., Gillespie, P., Pollard, D.D., 2001. Effect of local stress perturbation on secondary fault development. Journal of Structural Geology 24, 145–153.

Manighetti, I., Sammis, C., King, G., Campillo, M., 2003. Evidence for self-similar, triangular slip distributions on earthquake faults, and implications on fault and earthquake mechanics. Eos Transactions, American Geophysical Union, Fall Meeting Supplement, Abstract 84 (46), S21G-03.

Martel, S.J., Langley, J.S., 2006. Propagation of normal faults to the surface in basalt, Kaoe fault system, Hawaii. Journal of Structural Geology, in press, doi:10.1016/j.jsg.2005.12.004.

McClay, K.R. (Ed.), 1992. Thrust Tectonics. Chapman and Hall, New York, 447pp.

McKee, E.H., Duffield, W.A., Stern, R.J., 1983. Late Miocene and early Pliocene basaltic rocks and their implications for crustal structure, northeastern California and south-central Oregon. Geological Society of America Bulletin 94, 292–304.

Middleton, G.V., Wilcock, P.R., 1994. Mechanics in the Earth and Environmental Sciences. Cambridge University Press, Cambridge.

Mitra, G., Wojtal, S.F. (Eds.), 1988. Geometries and Mechanisms of Thrusting, with Special Reference to the Appalachians. Geological Society of America Special Paper 222, 236pp.

Mitra, S., 1990. Fault propagation folds; geometry, kinematic evolution, and hydrocarbon traps. American Association of Petroleum Geologists Bulletin 74 (6), 921–945.

Montgomery, S.L., 1988. Modoc Plateau: a question of origins. Petroleum Frontiers 5 (4), 1–44.

Moore, J.M., Schultz, R.A., 1999. Processes of faulting in jointed rocks of Canyonlands National Park, Utah. GSA Bulletin 111, 808–822.

Patton, T.L., Fletcher, R.C., 1995. Mathematical block-motion model for deformation of a layer above a buried fault of arbitrary dip and sense of slip. Journal of Structural Geology 17, 1455–1472.

Peacock, D.C.P., Parfitt, E.A., 2002. Active relay ramps and normal fault propagation on Kilauea Volcano, Hawaii. Journal of Structural Geology 24, 729–742.

Savage, H.M., Cooke, M.L., 2003. Can ramp-flat geometry be inferred from fold shape? A comparison of kinematic and mechanical folds. Journal of Structural Geology 25, 2023–2034.

Schlische, R.W., 1995. Geometry and origin of fault-related folds in extensional settings. American Association of Petroleum Geologists Bulletin 79, 1661–1678.

Schlische, R.W., Yound, S.S., Ackermann, R.V., Gupta, A., 1996. Geometry and scaling relations of a population of very small rift-related normal faults. Geology 24, 683–686.

Sharp, I.R., Gawthorpe, R.L., Underhill, J.R., Gupta, S., 2000. Fault-propagation folding in extensional settings: examples of structural style and synrift sedimentary response from the Suez rift, Sinai, Egypt. GSA Bulletin 112, 1877–1899.

Thomas, A.L., 1993. Poly3D: a three-dimensional, polygonal-element, displacement discontinuity boundary element computer program with applications to fractures, faults, and cavities in the Earth's crust. M.S. thesis, Stanford University, California.

Walsh, J.J., Watterson, J., 1987. Distributions of cumulative displacement and seismic slip on a single normal fault surface. Journal of Structural Geology 9, 1039–1046.

Walsh, J.J., Watterson, J., 1988. Analysis of the relationship between displacements and dimensions of faults. Journal of Structural Geology 10, 239–247.

White, I.R., 2003. Development of extensional fault propagation folds on the Modoc Plateau, northeastern California. M.S. thesis, Western Washington University, Bellingham, Washington, 112pp.

Willemse, E.J.M., Pollard, D.D., Aydin, A., 1996. Three-dimensional analyses of slip distributions on normal fault arrays with consequences for fault scaling. Journal of Structural Geology 18, 295–309.

Willsey, S.P., Umhoefer, P.J., Hilley, G.E., 2002. Early evolution of an extensional monocline by a propagating normal fault: 3D analysis from combined field study and numerical modeling. Journal of Structural Geology 24, 651–669.

Withjack, M.O., Olson, J., Peterson, E., 1990. Experimental models of extensional forced folds. American Association of Petroleum Geologists 74, 1038–1054.